Synchronous Ensembles of Hippocampal CA1 Pyramidal Neurons Associated with Theta but not Ripple Oscillations During Novel Exploration

En-Li Chen[1,2], Tsai-Wen Chen[1,2], Eric R. Schreiter[3], Bei-Jung Lin[1,2*]

[1]Institute of Neuroscience, National Yang Ming Chiao Tung University, Taipei, Taiwan
[2]Brain Research Center, National Yang Ming Chiao Tung University, Taipei, Taiwan
[3]Janelia Research Campus, Howard Hughes Medical Institute, Ashburn, VA 20147, USA.
*Corresponding author: beijunglin@nycu.edu.tw

Abstract

Synchronous neuronal ensembles play a pivotal role in the consolidation of long-term memory in the hippocampus. However, their organization during the acquisition of spatial memory remains less clear. In this study, we used neuronal population voltage imaging to investigate the synchronization patterns of CA1 pyramidal neuronal ensembles during the exploration of a new environment, a critical phase for spatial memory acquisition. We found synchronous ensembles comprising approximately 40% of CA1 pyramidal neurons, firing simultaneously in brief windows (~25ms) during immobility and locomotion in novel exploration. Notably, these synchronous ensembles were not associated with ripple oscillations but were instead phase-locked to local field potential theta waves. Specifically, the subthreshold membrane potentials of neurons exhibited coherent theta oscillations with a depolarizing peak at the moment of synchrony. Among newly formed place cells, pairs with more robust synchronization during locomotion displayed more distinct place-specific activities. These findings underscore the role of synchronous ensembles in coordinating place cells of different place fields.

Introduction

The establishment of long-term memory involves the initial acquisition and subsequent consolidation of memory traces, processes intricately connected to the modification of synaptic transmission[1,2]. Synchronous ensembles, characterized by the simultaneous firing of multiple neurons over tens of milliseconds (referred to as population synchrony), play a pivotal role in influencing synaptic plasticity[3-5]. The hippocampus, a crucial region for long-term memory formation[6,7], has been a focal point of synchronous ensemble studies. Within the hippocampus, synchronous ensembles are hypothesized to play roles in reactivating and consolidating labile memory traces[8]. However, their organization during memory acquisition remains less understood.

In the hippocampus, synchronous ensembles among CA1 pyramidal cells (CA1PCs) are predominantly observed during sharp-wave ripples, the brain waves associated with memory consolidation[8-13]. During these events, 10-18% of CA1PCs generate spikes, particularly during offline consummatory behavioral states or sleep[14,15]. These synchronous ensembles are biased toward experience-dependent reactivation, consolidating labile memory traces[16,17]. Furthermore, synchronous ensembles firing action potentials in short windows of 10-30 milliseconds enhance information processing[6] and discriminate distinct behavioral contingencies[18]. Although synchronous ensembles of CA1PCs during offline memory consolidation are well-characterized, their organization during online acquisition of spatial memory, such as when animals enter a new environment and new place cells form, remains unclear.

Previous studies have identified correlated activities among place cells during theta oscillation, where 1-3% of place cells' spikes co-activate in a forward order matching animals' trajectory in the theta cycles when animals' locations overlap in the place fields of these cells[19-21]. Because these place cells fire at distinct theta phases in the same cycle, this coordinated firing operates on the timescale of theta periods (~125ms)[22,23]. Population synchrony on shorter timescales (10-30 ms) is

53 speculated to be reduced by the presence of theta oscillations[22].

54

55 The subthreshold membrane voltage (subVm), influenced by synaptic inputs and intrinsic
56 conductances, directly triggers spiking activity[24,25]. Additionally, properties of subVm support the
57 organization of neuronal representation[26]. Although correlated membrane potentials have been
58 proposed to underlie the synchrony of neuronal ensembles[27,28], multicellular recordings of subVms
59 have not yet provided direct experimental evidence. Given the intricate interaction among subVm,
60 spiking, and place cell formation, it is crucial to investigate the temporal relationships of sub- and
61 suprathreshold neuronal activities among CA1PCs during novel exploration.

62

63 In this study, we used voltage imaging to investigate the temporal dynamics of sub- and
64 suprathreshold neuronal activities in CA1PCs during novel exploration. We found synchronous
65 ensembles involving approximately 40% of CA1PCs exhibited transient population synchrony and
66 correlated subthreshold membrane potentials when mice ran and stopped in a new maze.
67 Surprisingly, these synchronous ensembles occurred outside ripple episodes and were phase-locked
68 to extracellular and intracellular theta oscillations. Notably, cell pairs with stronger synchronous
69 activities established more distinct place fields that overlapped less. In essence, synchronous
70 ensembles facilitated temporal association among place cells representing diverse features of
71 spatial memory. This plastic network, driven by synchronous ensembles, may contribute to the
72 stabilization of place cells, establishing place fields that effectively tile the environment.

73

74 Results

75 To investigate the temporal relationships between neuronal activities during novel exploration, we
76 simultaneously recorded many neurons as animals explored a new environment for the first time.
77 To achieve this, we employed voltage imaging in conjunction with an air-lifted plastic track that
78 allowed mice to explore an environment while remaining head-fixed under a microscope (Figure

1A). To ensure a genuinely novel experience, all pre-training and habituation were performed in a separate room distinct from the one where the imaging experiments were conducted. On the day of imaging, the mice were introduced to the recording room for the first time and initially confined to a specific corner of the track (Figure 1A top view). Subsequently, as the imaging session commenced, the confinement was lifted, granting mice the freedom to explore the track while imaging was conducted.

In novel exploration, mice moved at a speed of 8.3±0.9 cm/s during locomotion (speed>3 cm/s) and spent 53±7% and 36±6% of their time in locomotion and immobility (speed<1 cm/s), respectively (n=5 mice). Meanwhile, they completed 10±2.5 laps during the 180-s imaging periods (n=5 mice).

For voltage imaging, we expressed the voltage indicator Voltron2[29] in CA1 pyramidal cells (CA1PCs), allowing us to measure both suprathreshold and subthreshold membrane potentials from multiple CA1PCs (14±4 cells imaged per field of view (mean±s.d.) and, in total, 71 cells imaged from 5 fields of view in 5 mice; Figure 1B). Simultaneously, we monitored the animals' positions and speed within the track while recording the local field potential (LFP) from the contralateral side of the hippocampus.

The mean firing rates of cells ranged from 2.3 to 4.3 Hz (25th-75th percentiles) with a median of 3.2 Hz (n=71 cells, Supplementary Figure 1A). Additionally, most CA1PCs exhibited elevated mean firing rates during immobility relative to locomotion, and their firing rates showed a negative correlation with the animals' speed (Supplementary Figure 1B and 1C), consistent with previous research[30].

Synchronous ensembles among many CA1 pyramidal neurons

Figure 1C shows the fluorescence traces of all neurons in a session as an example. Instances of synchronous activity, where many neurons emitted spikes within a narrow time window, were frequently observed (Figure 1C). To investigate synchronous activity within the neuronal population,

we selected a reference cell and counted the number of spikes across all other cells that were aligned with the spikes of the reference cell. This approach yielded a grand average cross-correlogram (CCG) capable of elucidating the timing of spikes from the reference cell relative to the combined spikes of the rest of the population. Notably, the grand average CCG exhibited heightened spike counts around zero lags, unlike flattened counts calculated from randomly selected cells of different sessions (Figure 1D and 1E). The full width at half maximum (FWHM) of the peak in the grand average CCG measured 23±14 ms (mean±s.d., n=71 cells from 5 sessions; Figure 1F), indicating the timescale of the population synchrony. Furthermore, pairwise CCGs of many cell pairs showed significant peaks compared to jittered data (percentage of significant pairs: 63%, median, n=497 pairs, Figure 1-figure supplement 1A and 1B). Among pairs with significant peaks, the absolute values of the peak lags ranged from 0.8 to 4.3 ms (25th-75th percentiles) with a median of 2.1 ms, and the FWHM of the peaks ranged from 20 to 46 ms (25th-75th percentiles) with a median of 30 ms (n=315 pairs, Figure 1-figure supplement 1C and 1D). These results highlight the synchronous spiking between neurons on the millisecond timescale.

To systematically reveal individual synchronous events, we counted the number of spikes from all simultaneously recorded neurons within sliding windows of 25 ms. To compare the summed spikes with controls, we randomly jittered the spike trains to perturb spike timings while maintaining spike rates. We identified moments of population synchrony when spike sums exceeded the average of the jittered spike sums plus four standard deviations (Figure 1C). Using the same criterion for event detection, we observed over a 7.8-fold increase in synchronous events in original data compared to jittered controls (mean event rate: 0.94±0.17 Hz for the original data, 0.12±0.01 Hz for the jittered data, n=10 segments, p=0.002, Wilcoxon signed-rank test; Figure 1G). Furthermore, we calculated the percentage of neurons participating in these synchronous events to examine the synchronous ensemble sizes. The ensemble sizes ranged from 32% to 53% (25th-75th percentiles) with a median of 42%, which were larger than the synchronous ensemble sizes associated with ripples[14] (Figure

1H). These results demonstrate synchronous ensembles of CA1PCs engaging many neurons.

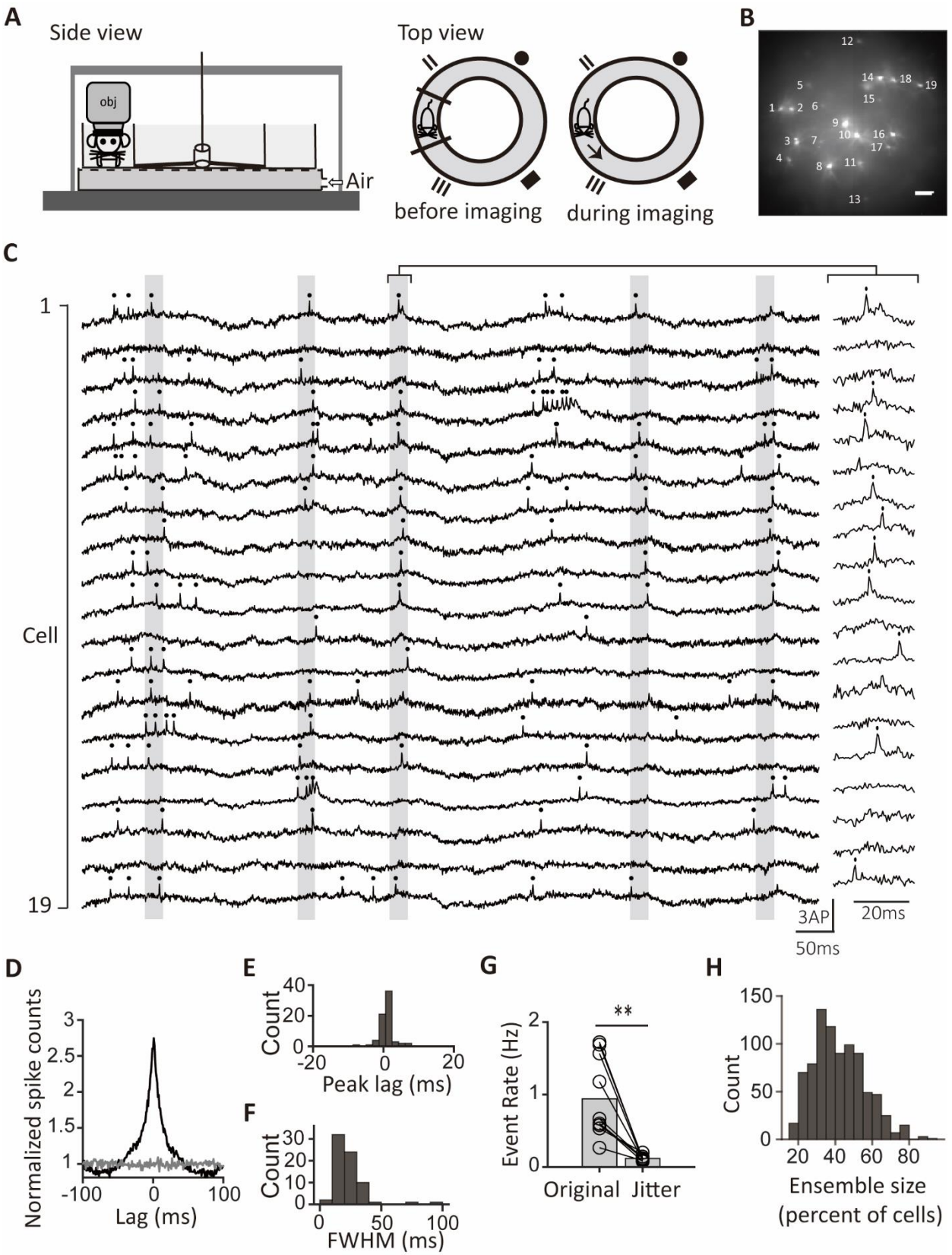

Figure 1 Population synchrony during novel exploration.

136 **(A)** Schematic of the behavioral setup for voltage imaging. Mice explored a novel one-way track
137 while fluorescence images were captured at the CA1 pyramidal layer. Left: side view; right: top view
138 of the setup.
139 **(B)** Example time-averaged image of CA1 pyramidal cells expressing Voltron2-ST labeled with JF_{552}-
140 HaloTag ligand. Scale bar, 100 μm.
141 **(C)** Fluorescence traces of cells in an example session with identified synchronous ensembles
142 (labeled with gray vertical bars). Right: an example of magnified fluorescence traces within the
143 bracket, pinpointing the occurrence of the identified synchronous ensemble. Spikes are indicated by
144 dots on the top.
145 **(D)** The grand average cross-correlogram (CCG) averaged across all 71 cells. The gray line represents
146 the mean grand average CCG between reference cells and randomly selected cells from different
147 sessions.
148 **(E)** Distribution of the grand average CCG peak lags of all cells (n=71).
149 **(F)** Distribution of the full width at half maximum (FWHM) of the grand average CCGs (n=71 cells).
150 **(G)** Pairwise comparison of the event rates of population synchrony between original and jittered
151 data. Bar heights indicate group means. **p<0.01
152 (**H**) Histogram of the ensemble sizes as percentages of cells participating in the synchronous
153 ensembles.
154
155
156 **Synchronous ensembles during locomotion and immobility of novel exploration**
157 The hippocampus exhibits state-dependent activities when rodents are engaged in locomotion and
158 immobility[30,31]. In novel exploration, CA1PCs showed synchronous spiking during locomotion and
159 immobility (Figure 2A). To investigate whether these synchronous activities differed between these
160 behavioral states, we compared grant average CCGs and synchronous ensembles under these
161 conditions. During both immobility and locomotion, grant average CCGs showed prominent peaks

compared to jittered data (Figure 2B). Moreover, synchronous ensembles were rich in both immobility and locomotion periods (Figure 2A, 2B and 2D). Nevertheless, the FWHMs of grant average CCGs were broader in the immobility group compared to the locomotion group (Figure 2B and 2C). Synchronous events occurred more frequently during immobility compared to locomotion (Figure 2D). Additionally, ensemble sizes were significantly larger in the immobility group compared to the locomotion group (Figure 2E). Taken together, with differences in sizes and kinetics, there were synchronous ensembles during both immobility and locomotion periods of novel exploration.

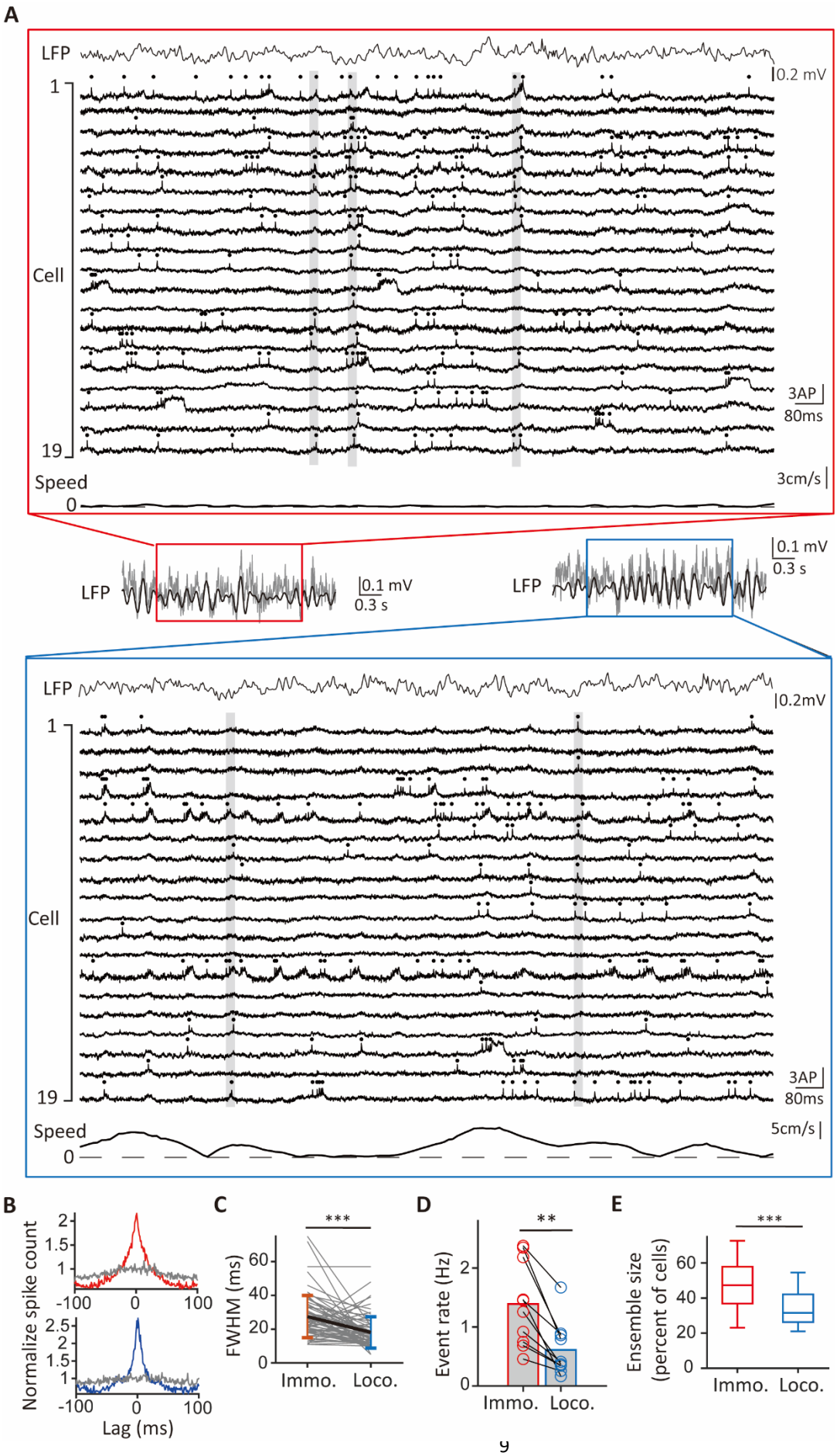
A
LFP
0.2 mV
1
Cell
19
3AP
80ms
Speed
0
3cm/s
LFP
0.1 mV
0.3 s
LFP
0.1 mV
0.3 s
LFP
0.2mV
1
Cell
19
3AP
80ms
Speed
0
5cm/s
B
Normalize spike count
Lag (ms)
C
FWHM (ms)
Immo.
Loco.
D
Event rate (Hz)
Immo.
Loco.
E
Ensemble size (percent of cells)
Immo.
Loco.

169

Figure 2 Comparison of synchronous ensembles between immobility and locomotion.

(A) Example traces of cells in a session with identified synchronous ensembles (gray rectangles) during periods of immobility (red rectangular frame) and locomotion (blue rectangular frame). Spikes are indicated by dots at the top of individual traces. Top: the simultaneously recorded LFP trace. Bottom: simultaneously recorded speed of the animal. Inset: the band-pass filtered LFP trace at the theta frequency range (black line) overlaid on the raw LFP trace (gray line).

(B) The grand average cross-correlograms (CCGs) during immobility (red) and locomotion (blue) averaged across all cells (n=71). The gray lines represent the mean grand average CCGs calculated from jittered data.

(C) Pairwise comparison of peak widths (FWHM) in the grand average CCGs between immobility (red) and locomotion (blue). Vertical bars represent means and standard deviations for both groups (FWHM: 27±12 ms for immobility, 18±9 ms for locomotion, mean±s.d., $p<0.001$, paired Student's *t*-test, n=71 cells). ***$p<0.001$

(D) Pairwise comparison of event rates of population synchrony during immobility and locomotion. Bar heights indicate group means (immobility: 1.4±0.7 Hz, locomotion: 0.6±0.5 Hz, mean±s.d., n=10 segments, $p=0.002$, Wilcoxon signed-rank test). **$p<0.01$

(E) Boxplot of ensemble sizes for synchronous ensembles occurring during immobility (red) and locomotion (blue) (median ensemble size: 47% for immobility, n=446 events, 32% for locomotion, n=313 events, $p<0.001$, Wilcoxon rank-sum test). ***$p<0.001$

Synchronous ensembles occur outside ripple episodes

CA1PCs exhibit synchronous activities when the hippocampal network emits ripple waves[8,14]. To test whether there is a co-occurrence of synchronous ensembles and ripples, we first detected ripples from LFP recordings. Ripples were detected in three of the five recording sessions, and all occurred during immobility (mean ripple rate: 0.04±0.02 Hz during immobility, 0 Hz during locomotion). In

196 the two recording sessions where we did not detect any ripples, we verified the recording quality of
197 the LFP signal by running multiple tests after the recording sessions. Ripples were identified in the
198 same animals during quality tests, indicating that the absence of ripples during novel immobility in
199 the recording session was not due to the deterioration of LFP recordings (Figure 3-figure
200 supplement 1).
201
202 To visualize both ripples and synchronous ensembles, we plotted voltage traces of neurons
203 alongside simultaneously recorded ripple oscillations. It was typical for synchronous ensembles to
204 occur far away from ripple episodes (Figure 3A). To delve into the relationship between neuronal
205 activities and ripples, we aligned traces of ripple power with population synchrony and ripples. In a
206 recording session where 64 synchronous ensembles and 12 ripples were detected during
207 immobility, the LFP power at ripple frequency (120-240 Hz) exhibited no discernable peaks within
208 any of the synchronous events (Figure 3B, left upper and middle panels). Nevertheless, the same
209 LFP power displayed substantial peaks during every ripple event (Figure 3B, right upper and middle
210 panels). A striking contrast between synchronous events and ripples was also evident when spiking
211 probabilities during these events were examined. During population synchrony, the mean spiking
212 probability averaged across all cells was high, while the spiking probability was almost zero during
213 ripple events (Figure 3B lower panel). In the three sessions where ripples were identified, we
214 calculated the percentages of ripple events coinciding with synchronous ensembles and vice versa.
215 Remarkably, there was no co-occurrence of ripples and synchronous ensembles (Figure 3C).
216 Furthermore, we quantified ripple-modulated spiking by calculating the ratio of the difference in
217 mean firing rates during in-ripple and out-ripple periods to the sum of the mean firing rates during
218 both periods. Indexes of most cells were negative, and a striking 85% of cells displayed ripple
219 modulation indexes of -1, indicating complete suppression of their spiking activities during ripples
220 (Figure 3D). Taken together, during novel exploration, synchronous ensembles involved many
221 neurons with millisecond-synchronized spikes and occurred outside the time frames of ripples.

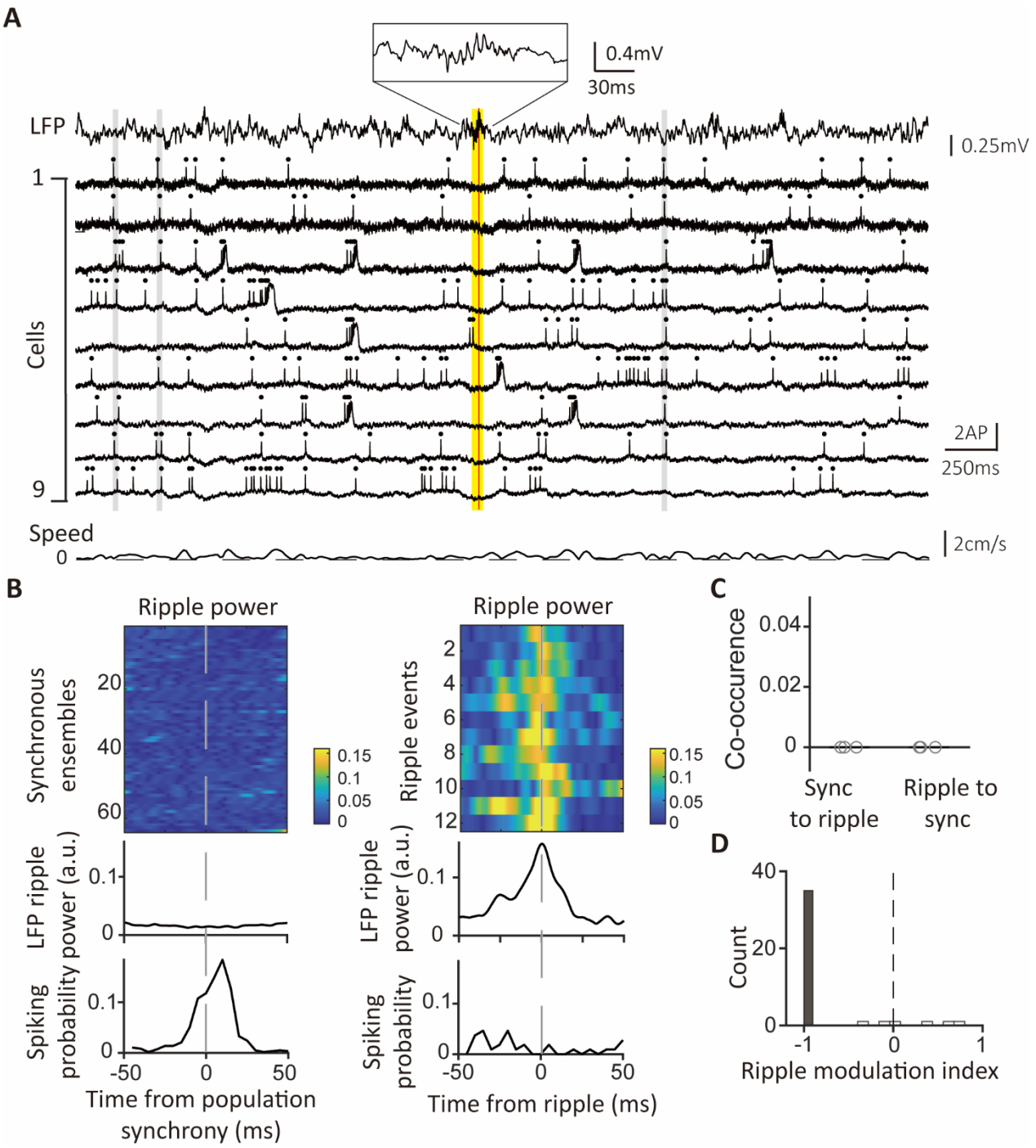

Figure 3 Synchronous ensembles occur outside ripple episodes.

(A) Example traces with ripples and synchronous ensembles. Top: simultaneously recorded LFP displaying an episode of ripple oscillation. A red vertical line indicates the timing of the peak ripple power in the LFP trace. A yellow rectangle marks the duration of the ripple episode. Inset at the top: a magnified view of the ripple oscillation. Middle: fluorescence traces of 9 CA1PCs. Gray rectangles

229 mark the timings of the synchronous ensembles on all traces. Bottom: animals' speed recorded
230 simultaneously with voltage imaging.
231 **(B)** LFP ripple power and spiking probability aligned to synchrony ensembles and ripple events.
232 Upper panel: color-coded LFP power at ripple frequency (120-240Hz) aligned to the timings of 64
233 synchronous ensembles (left) and 12 ripple events (right). Middle panel: Average LFP power of
234 ripple frequency aligned to the timings of the synchronous ensembles (left) and the ripple events
235 (right). Lower panel: Average spike counts of all cells aligned to the timings of the synchronous
236 ensembles (left) and ripple events (right).
237 **(C)** Percentages of co-occurrences between population synchrony and ripples. The co-occurrences
238 in the "sync to ripples" group represent the percentages of ripple episodes co-occurring with
239 synchronous ensembles in the same episodes. The co-occurrences in the "ripples to sync" group
240 indicate the percentages of synchronous ensembles co-occurring with ripple episodes. Each gray
241 circle represents an individual session.
242 **(D)** Distribution of the ripple modulation indexes (n=41 cells). Gray bar: modulation indexes with
243 significant p values (n=35 cells); white bars: modulation indexes without significance (n=6 cells).
244
245
246 **Synchronous ensembles are associated with theta oscillations**
247 To investigate the network dynamics associated with synchronous ensembles, we aligned LFP traces
248 triggered by the timings of synchronous ensembles. The average LFP traces of a representative
249 session showed prominent theta oscillations around the timings of both immobility and locomotion
250 population synchrony (Figure 4A). Spectral analysis of the mean synchrony-triggered LFP traces
251 during immobility and locomotion revealed theta frequency components of 4-12 Hz, with a slightly
252 higher peak frequency in locomotion LFP compared to immobility LFP (Figure 4B). Furthermore, we
253 computed LFP theta modulation and identified preferred phases of synchronous ensembles. In line
254 with the previous result, synchronous ensembles displayed a high level of modulation by LFP theta

oscillation (modulation strength: 0.61±0.05 during immobility and 0.74±0.04 during locomotion, n=5 sessions). Although the preferred phases varied from session to session due to differences in recording sites along the proximal-distal axis of the hippocampus, the timings of individual ensembles were consistently locked to the preferred phase of each session (Figure 4C). These results establish a strong link between synchronous ensembles and LFP theta oscillation.

Subthreshold membrane voltage (subVm) is one of the critical parameters supporting the generation of action potentials. To investigate the subthreshold signals underlying population synchrony, we aligned subVm traces with the timings of synchronous ensembles and observed that both immobility and locomotion synchrony rode on a subVm waveform oscillating at theta frequency (Figure 4D). To elucidate further the relationship between subVm theta oscillation and spikes involved in population synchrony, we calculated the subVm theta modulation and preferred phases of spikes. Spikes participating in both immobility and locomotion synchrony were strongly coupled to the subVm theta oscillation of neurons, with the mean preferred phase being in the latter half of the rising phase closer to subVm theta peaks (Figure 4E). Conversely, spikes not participating in synchronous ensembles had weaker modulation strength compared to spikes involved in synchrony (Figure 4-figure supplement 1A and 1B). Furthermore, the membrane voltages triggered by these two categories of spikes showed a significant difference in the hyperpolarization phase of the theta oscillation. Synchronous spikes were situated within cycles of theta oscillations featuring more hyperpolarized troughs than spikes outside synchronous ensembles (Figure 4-figure supplement 1C and 1D). Thus, compared to spikes not participating in synchronous ensembles, synchronous spikes showed a more robust modulation by theta oscillation of membrane voltage during immobility and locomotion in the context of novel exploration.

Notably, phase locking of spikes to their subVm theta oscillation and the synchronous spikes among many neurons suggest that subVms of different neurons would be correlated at the theta frequency.

281 To explore the possibility, we divided the 180-second subVm traces into 1-second segments with
282 50% overlap and calculated the cross-correlation and magnitude-squared coherence function for
283 each pair of cell segments. Segments were sorted into the immobility or locomotion group based on
284 the animals' speed during each segment (kept below 1 cm/s for immobility and above 3 cm/s for
285 locomotion for more than 90% of the time). In total, we analyzed 511 cell pairs from 5 sessions.
286 Indeed, the cross-correlation of subVm between cell pairs revealed a high correlation at zero lag and
287 periodic modulation of the correlation at theta frequency (Figure 4F). Furthermore, the subVm
288 theta coherences were increased in both groups (immobility: 0.50, locomotion: 0.40, median,
289 n=511 pairs) and were negatively correlated with soma distances (immobility: -0.46, locomotion: -
290 0.48, n=511 pairs, Figure 4G). Taken together, during novel exploration, CA1PCs generate
291 synchronous activity associated with theta oscillation and exhibit correlated and theta-coherent
292 subVms.
293

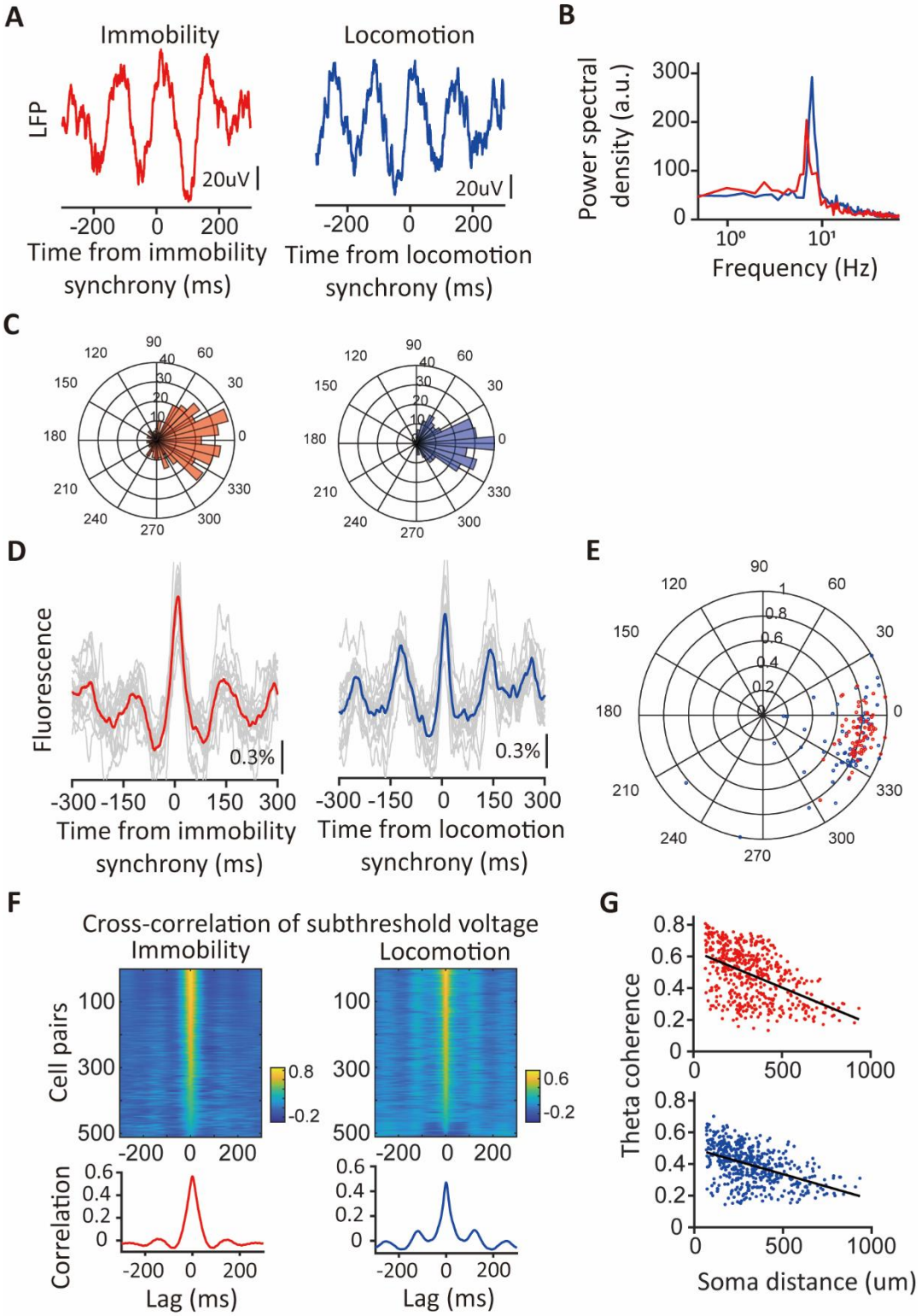

Figure 4 Theta oscillations in the LFP and subthreshold membrane potential were linked to population synchrony.

(A) LFP waveforms triggered by timings of synchronous ensembles. Red: triggered by timings of immobility synchrony; blue: triggered by timings of locomotion synchrony.

(B) Power spectral densities of the triggered LFP waveforms. Red: immobility; blue: locomotion.

(C) Distributions of the differences between LFP theta phases of individual synchronous ensembles and their preferred phases of the session. Note that most ensembles show minor differences within ±30 degrees. Red: immobility; blue: locomotion.

(D) Fluorescence traces triggered by timings of synchronous ensembles. Traces with spikes are excluded. Left panel: traces triggered by timings of immobility synchrony. Right panel: traces triggered by timings of locomotion synchrony. Thin gray lines: mean triggered fluorescence traces averaged across triggers for representative cells. Thick red and blue lines: mean triggered fluorescence traces averaged across cells.

(E) Polar plot illustrating theta modulation of spikes participating in the immobility synchrony (red dots) and of spikes participating in the locomotion synchrony (blue dots). The angle of the dots indicates the preferred phase, and the distance from the center of the circle represents the modulation strength. Each dot represents the averages from a neuron.

(F) Pairwise cross-correlation of the subthreshold membrane voltages (subVm). Top: color-coded cross-correlation of subVm between cell pairs during immobility and locomotion periods. Bottom: averaged cross-correlation over all cell pairs for immobility (red) and locomotion (blue) subVm. Both show a central peak at zero lag flanked by theta oscillation.

(G) Scatter plots of theta coherence against soma distances of immobility subVm (red) and locomotion subVm (blue) between cell pairs.

318 **Synchrony between place cells with distinct place tunings**

319 When animals explore a novel maze, spatially tuned spiking activity can form within a few
320 minutes[32,33]. However, how synchronous ensembles organize their spatially tuned activities during
321 novel exploration remains to be determined. Synchronous ensembles, generating spikes
322 coincidently in short intervals, might display correlated spiking at longer time windows that match
323 behavioral timescales of exploration, potentially leading to shared place responses. On the other
324 hand, CA1PCs are interconnected through inhibitory interneurons[34-36]. Modulation of activities in
325 inhibitory interneurons by some place cells may influence the activities of other place cells,
326 resulting in divergent spatial tunings[32,37,38].

327

328 To compare the spatial tunings of synchronous cell pairs, we first calculated the spatial tuning
329 curves of individual neurons by computing the mean firing rates in every spatial bin. On average,
330 40% of cells displayed selective spatial tunings of their spiking activities and were qualified as place
331 cells[39] (Figure 5A). Among place cell pairs, some showed similar spatial tunings, while others did not
332 (Figure 5B). For instance, in an illustrative session depicted in Figure 5B, the seventh and eighth
333 place cells had highly similar spatial tunings with a correlation coefficient as high as 0.7. In contrast,
334 the fifth and tenth place cells exhibited vastly different spatial tunings with a correlation coefficient
335 as low as -0.5.

336

337 We further explored the relationship between the similarity of spatial tunings and synchronization
338 strength among pairs of place cells. We measured synchronization strength as the peak of the CCG
339 normalized by the averaged jittered spike count within the same bin as the CCG peak. We
340 segregated spikes based on these behavioral states to accommodate differences between
341 locomotion and immobility and calculated the corresponding CCG and synchronization strength.

342

343 During locomotion, we observed a robust negative correlation between synchronization strength

344 and the similarity of spatial tunings among cell pairs. In other words, cell pairs with more precisely
345 co-active spikes during locomotion exhibited more distinct place-tuning profiles (Figure 5C and 5D).
346 This anti-correlation between synchronization strength and place tunings indicates coordination
347 between place cells' temporal and spatial coding. On the other hand, synchronization strength
348 during immobility showed little correlation with the similarity of spatial tunings among place cell
349 pairs, suggesting that correlated activities at the millisecond timescale do not extend to slow,
350 behavioral-relevant timescales (Figure 5-figure supplement 1). Thus, place cells with distinct place
351 fields are linked by synchronous activity during novel locomotion.
352

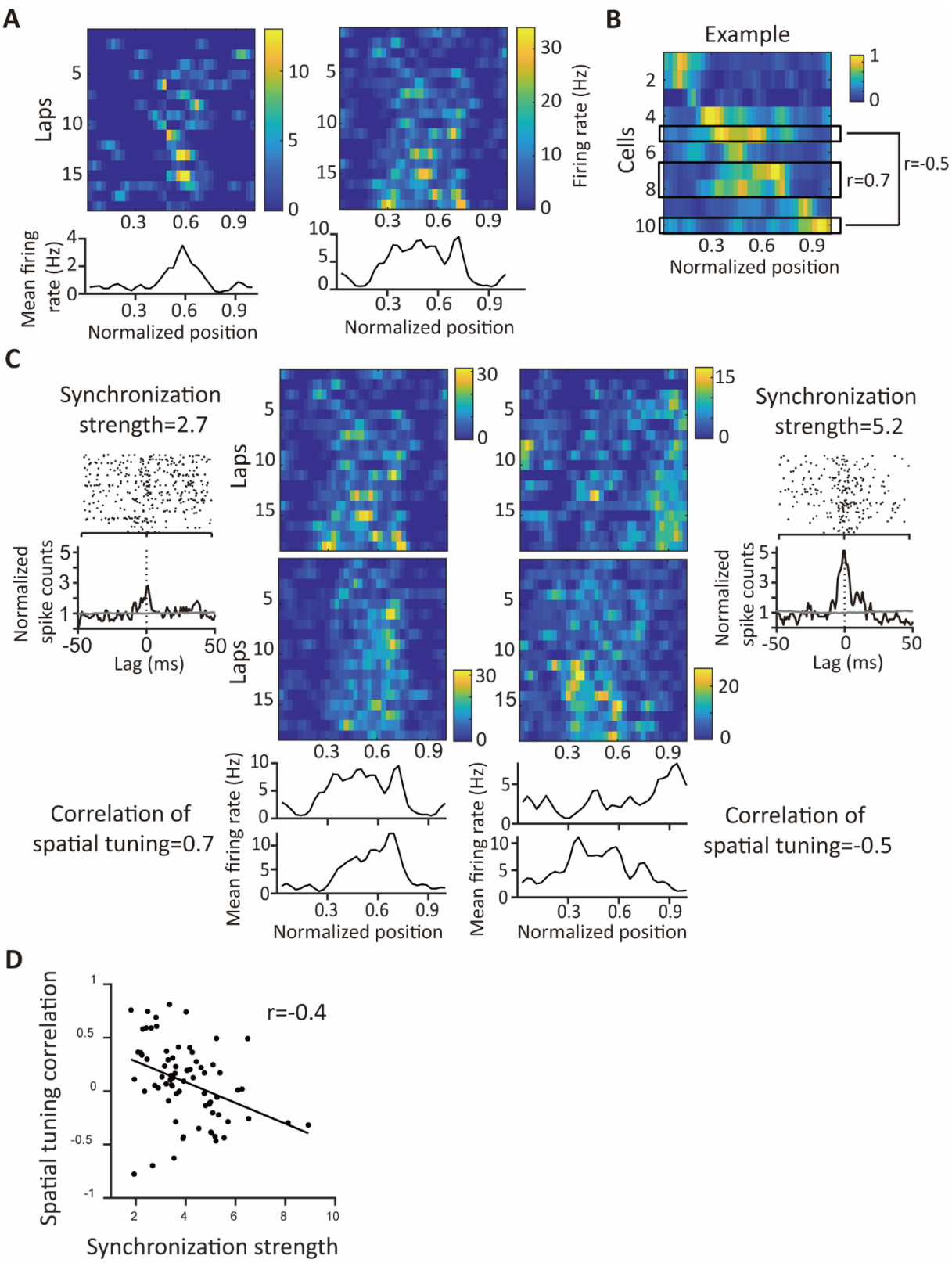

Figure 5 Negative correlation between spatial tuning similarity and synchronization strength during novel exploration.

(A) Spatially binned rate maps of place cells. High firing rates are indicated in yellow, and low firing

rates are noted in blue. Bottom: the mean firing rates along spatial bins averaged across laps.

(B) Spatial tunings of 10 place cells from an example session. Cells are sorted based on the locations of their peak firing rates.

(C) Two example pairs of neurons with cross correlograms during locomotion and spatially binned firing rate maps.

(D) A scatter plot of correlation coefficients of spatial tunings against synchronization strengths for place cell pairs. Each dot represents a pair of place cells. Synchronization strengths are negatively correlated with similarities of spatial tunings (Spearman correlation coefficient=-0.4, $p<0.001$, n=73 pairs).

Discussion

Our findings reveal the presence of synchronous ensembles comprising a substantial number of CA1PCs during both locomotion and immobility in a novel environment. These ensembles concurrently engage neurons representing diverse aspects of the environment and are rarely observed during ripple events. Instead, they closely align with LFP and intracellular theta oscillations. Our data demonstrate theta-associated synchronous ensembles during spatial memory acquisition, coordinating numerous CA1 place cells that transmit information about different segments of the environment.

The correlation between observed population synchrony and theta oscillations is intriguing. Theta oscillations are typically associated with the sequential activation of neurons over time, resulting in reduced neuronal synchrony[22]. However, theta oscillations come in different types, each characterized by distinct pharmacological properties and behavioral correlates[40-42]. For example, type 1 theta, referred to as translational theta, occurs during voluntary movements and is sensitive to N-methyl-D-aspartate receptor (NMDAR) blockers. On the other hand, type 2 theta, known as

383 attentional theta, is blocked by muscarinic receptor antagonists, emerging during states of arousal
384 or attention, such as entering a new environment[43-45].
385
386 During theta oscillations, cholinergic neurons in the medial septum excite downstream CA1PCs,
387 leading to increased firing rates and membrane potentials[46-48]. Given the widespread influence of
388 cholinergic inputs on numerous CA1PCs, theta-coupled cholinergic inputs may drive depolarization
389 and firing across many CA1PCs. Additionally, they could enhance the likelihood of synchronicity.
390 Furthermore, GABAergic neurons in the medial septum, activated during theta oscillations, could
391 activate interneurons in the CA1 region[42,49,50]. These CA1 interneurons, in turn, have the capability
392 to entrain the activities of pyramidal neurons at both sub- and suprathreshold levels, thereby
393 promoting synchronization among pyramidal neurons[51,52]. In summary, cholinergic and GABAergic
394 neuron activation during theta waves may contribute to the excitation of CA1PCs and the
395 consequent increase in their synchronicity.
396
397 Theta oscillations have long been implicated in memory acquisition. Specifically, theta power
398 correlates positively with learning performance[53-55]. Perturbing generation of theta waves leads to
399 impairment in memory acquisition[56-60], while electrical stimulation restoring theta rhythms rescues
400 learning performance[61,62]. Furthermore, increased spike-theta coherence correlates with better
401 memory, and stimulations that boost theta phase-locking of spikes enhance memory[63-65]. Despite
402 abundant evidence supporting a link between theta oscillations and memory, the precise network
403 mechanism by which theta oscillations support memory acquisition remains unclear. Theta
404 oscillations are hypothesized to link spatially distributed neurons into functional ensembles to
405 support memory acquisition[13]. The identified synchronous ensembles support the hypothesis,
406 providing a network substrate that links theta rhythms to the initial stage of memory acquisition.
407
408 Previous reports of CA1 synchronous ensembles occur predominantly during ripple
409 oscillations[8,14,17]. However, we found only a few ripple events in the initial minutes of entering a

410 new environment, even when animals are not moving. During these events, CA1PCs show
411 decreased spiking activities, and they display synchronous firing outside ripple episodes (Fig.3).
412 Different from the ripple-associated synchronous ensembles described previously, the synchronous
413 ensembles we observed involve larger populations of neurons spiking synchronously in narrower
414 time intervals and are associated with theta oscillations. The absence of recorded ripple-associated
415 synchrony in our study may be attributed to elevated arousal with prominent theta oscillations even
416 during immobility, potentially suppressing ripples[66]. Additionally, the deep-layer CA1PCs imaged in
417 our study are known to show decreased activities during ripples, contributing to their lack of ripple-
418 associated synchrony[67]. The CA1 network may generate multiple types of population synchrony,
419 with ripple-associated synchrony facilitating memory consolidation, while the newly identified theta
420 population synchrony supports the initial stage of memory acquisition.
421
422 Although CA1PCs are known to exhibit weaker recurrent connectivity than that of CA3 pyramidal
423 neurons, CA1PCs did communicate through monosynaptic connections[68]. These connections can be
424 dynamically adjusted by the spike-timing-dependent plasticity mechanism[69-71], and therefore could
425 be affected by the transient population synchrony. In addition, CA1PCs are known to communicate
426 through inhibitory interneurons. Multiple pyramidal neurons converge onto a single interneuron,
427 and individual connections are often weak and unreliable[35,72,73]. This connectivity scheme requires
428 multiple pyramidal neurons spiking synchronously within the time window of synaptic integration to
429 effectively activate postsynaptic neurons[35]. Furthermore, population synchrony among CA1PCs may
430 propagate to downstream areas, synchronizing neurons outside the hippocampus. With their large
431 ensemble sizes, these synchronous ensembles may synergistically convey relevant information or
432 reorganize the connectivity of the neuronal networks.
433
434 Prior studies in sensory systems have commonly revealed that neurons with synchronous activities
435 typically share similar sensory responses[74,75]. However, the synchronous ensembles we have

436 identified often encompass neurons with distinct preferences for place fields. Pairwise synchrony
437 demonstrates a negative correlation with place field overlap (Fig. 5). These findings indicate that
438 synchrony does not necessarily imply similar tunings between neurons. Furthermore, these
439 synchronous ensembles involve place cells encoding different spatial information. Recognizing the
440 crucial role of neuronal synchrony in binding distributed neurons in the brain[3,5], population
441 synchrony may serve as a mechanism to integrate diverse features of the same environment into a
442 cohesive mental map.
443
444

445 # Methods

446 **Animal**

447 Time-pregnant wild-type C57BL/6J female mice underwent in utero virus injection of CamkII-cre
448 virus (105558-AAV1, Addgene) into the left side of the lateral ventricles. The resulting offspring
449 were raised in a breeding room under controlled temperature and humidity conditions and a 12-
450 hour light/dark cycle (lights on from 7:00 to 19:00). The mice used in the experiments were
451 between 12 and 18 weeks old at the time of the recordings. All surgical procedures, behavioral
452 training, and recording protocols were approved by the NYCU Institutional Animal Care and Use
453 Committee.

454

455 **In-utero virus injection**

456 Time-pregnant mice on an embryonic day 14.5 were anesthetized with isoflurane (induction:4-5%;
457 maintenance:1-3%) before surgery. The animals were placed on a heating pad in a supine position
458 to maintain body temperature. Aseptic procedures were implemented to maintain sterile conditions
459 during the surgery. Uterine horns were exposed one at a time using spoons and fingers. Warm and
460 sterile phosphate-buffered saline (PBS) was used to rinse the uterus to prevent it from drying out.
461 Micropipettes loaded with CamkII-cre virus solution were used to inject 0.2 uL of virus suspension
462 into the left side of the lateral ventricle of each embryo. The uterine horn was then gently returned
463 to the abdominal cavity. The exact process was repeated to the other uterine horn. After the
464 surgery, ketorolac (6mg/kg) and cefazolin (1g/kg) were administered for two days to minimize pain
465 and inflammation.

466

467 **Cranial window and cannula implantation**

468 The offspring of the mice that had undergone in-utero injection were subjected to chronic
469 hippocampal window surgery when they were between 2 and 4 months old. The animals were

470 initially anesthetized using isoflurane (induction:4-5%; maintenance:1-3%). Topical anesthesia was
471 applied by administering 0.5% lidocaine to the wound margins. After achieving deep anesthesia, an
472 incision was made in the skin, and a circular section of the skull was removed, centered 2 mm
473 caudal and 1.8 mm left to the bregma. Using 30-gauge needles and forceps, the dura was removed
474 from the exposed area, and cortical tissue within the craniotomy was aspirated. A fine injection
475 pipette (tip diameter 10-60 um) was used to inject AAV2/1-CAG-flex-Voltron2-ST ($2.7x10^{12}$ GC/ml, a
476 courtesy gift from Dr. Eric Schreiter and the GENIE team at HHMI Janelia Research Campus) into the
477 exposed regions at a depth of 200 μm (up to six injection sites and 100-200 nL of viral
478 suspension). An optical chamber was constructed by placing a cannula with a cover slip attached at
479 the bottom over the craniotomy and sealing it with dental acrylic or C&B Metabond (Sun Medical).
480 A custom-built titanium frame was then cemented to the animal's head using dental acrylic or C&B
481 Metabond. Mice received ketorolac (6mg/kg) and cefazolin (1g/kg) for two days following surgery to
482 minimize pain and inflammation.
483
484 **Behavioral training**
485 After at least two weeks of recovery from the window surgery, the mice underwent behavioral
486 training to ensure they were calm and attentive in the test environment. The initial training phase
487 involved acclimating the mice to head fixation and treadmill running, which took place over 3-5 days
488 in a separate room distinct from the recording setup. Following this training, the imaging
489 experiments were conducted. On the day designated for imaging, the mice were introduced to the
490 recording room for the first time just before the imaging session. During the imaging experiments,
491 the mice were securely held in a head-fixed position beneath the microscope and on an air-lifted
492 plastic track that rested on an air table (AirLift, Neurotar; Fig. 1Aa). The track was adorned with
493 various shapes of signs to help the mice navigate the track. Subdued blue lighting was provided to
494 illuminate the track. Before the initiation of imaging, the mice were confined in a corner of the track
495 using gates. Subsequently, the gates were opened upon the start of imaging, allowing the mice to

496 explore the new environment during their initial laps (Fig. 1Ab). The Mobile HomeCage tracking
497 system (Neurotar) was used to track the mice's position and speed. During the acquisition of image
498 frames, TTL pulses were sent by the high-speed camera to the Mobile HomeCage tracking system to
499 facilitate data alignment.
500
501 **Voltage imaging**
502 Imaging was performed after treadmill training. JF_{552}-HaloTag ligand[76] (a courtesy gift from Dr. Luke
503 Lavis) was first dissolved in DMSO (Sigma) and then diluted in Pluronic™ F-127 (P3000MP,
504 Invitrogen) and PBS to achieve a final concentration of 0.83 mM of JF_{552}-HaloTag ligand. The
505 solution was then injected intravenously through the retro-orbital sinus. Imaging sessions were
506 initiated 3-5 hours after the injection of the JF_{552}-HaloTag ligand. Fluorescence sensors were excited
507 using a 532-nm laser (Opus 532, Laser Quantum) with an excitation filter (FF02-520-28, Semrock),
508 and the emitted light was separated from the excitation light using a dichroic mirror (540lpxr
509 Chroma) and passed through an emission filter (FF01-596183 Semrock). A 16X, 0.8 NA objective
510 (Nikon) was used to collect the emission light which was then imaged on a CMOS camera (DaVinci-
511 1K, RedShirt) with a 50-mm camera lens (Nikkor 50mm f1.2, Nikon) as the tube lens. Images were
512 acquired using Turbo-SM64 (Sci-Measure) at 2kHz with a resolution of 190 x 160 pixels,
513 corresponding to a field of view of 1.4 x 1.2 mm. The number of frames in an image session was set
514 at 360,000, corresponding to a duration of 180 seconds per session. Imaging depths ranged
515 between 70 and 170 μm from the window surface, where the CA1 pyramidal neurons were
516 located. Time-lapse images were collected, and image stacks of the same field of view along the z-
517 axis were acquired. The image stacks consisted of 100 plans separated by two μm, covering the
518 depth from the window surface to 200 um from the surface.
519
520 **LFP recording**
521 The LFP signal from the contralateral CA1 region of the hippocampus was simultaneously recorded

522 during voltage imaging. To implant the LFP electrode, a small craniotomy was performed at the
523 dorsal CA1 coordinate (2mm caudal and 1.8 mm right to the bregma). A tungsten electrode
524 (#100211, 38 μm in diameter, polyimide insulated, California Fine Wire) was inserted into the
525 dorsal CA1 region, and the wire and pins were cemented in place with dental acrylic. The electrical
526 signal was amplified and filtered (1-1kHz) using a DAM80 amplifier (Word Precision Instruments).
527 The amplified signal was acquired by an I/O device (National Instruments USB-6341) and recorded
528 using WaveSurfer (Adam Taylor, HHMI Janelia Research Campus) at 10 kHz during implantation and
529 TurboSM64 (RedShirt) at 8 kHz during imaging.
530
531 **Voltage imaging preprocessing and spike detection**
532 Fluorescence intensities were corrected for brain movement using rigid registration. Regions of
533 interest (ROIs) were manually selected by grouping pixels that cover individual somata. The
534 fluorescence intensities of individual neurons were calculated by averaging the fluorescence
535 intensities of pixels from the same ROIs. Bleaching was corrected by calculating the baseline
536 fluorescence (F_0) at each time point as an average of the fluorescence intensities within $\pm$0.5 s
537 around the time point. The dF/F was calculated as the F_0 minus the fluorescence intensity of the
538 same time point divided by F_0. Positive fluorescence transients were detected to identify spikes
539 from the high-passed dF/F traces created by subtracting the dF/F traces from the median-filtered
540 version with a 5-ms window. To simulate the noise of recordings, high-passed dF/F traces were
541 inverted, and the amplitudes of the transients detected from the inverted traces were used to
542 construct a noise distribution of the spike amplitudes. A threshold was set by comparing the
543 amplitudes of the detected transients with the noise distribution of the spike amplitudes to
544 minimize the sum of type I and type II errors. Spikes were first detected when transients were larger
545 than the threshold. Then, spike amplitudes smaller than half of the top 5% spike amplitudes were
546 excluded. The signal-to-noise ratio (SNR) was calculated for each neuron as a ratio of the averaged
547 spike amplitudes over the standard deviation of the high-passed dF/F traces, excluding points 2 ms

548 before and 4 ms after each detected spike to estimate the quality of the recordings. The crosstalk
549 between ROIs was routinely checked by examining the refractory periods of neurons in auto-
550 correlograms. Only neurons meeting the following criteria were included: (1) SNR larger than 5, (2)
551 full width at half maximum of the spike waveform longer than 0.8 ms, (3) mean spike rates higher
552 than 0.1 Hz, (4) distances between soma pairs at least 70 μm. Sessions with at least nine neurons
553 meeting the selection criteria were used for further analysis. Based on these criteria, we included
554 five sessions containing 9, 11, 13, 19, and 19 neurons.
555
556 **Behavioral states of locomotion and immobility**
557 The periods of locomotion were defined as instances when the animals' speed exceeded 3 cm/s,
558 while periods of immobility were determined as instances when the animals' speed fell below 1
559 cm/s.
560
561 **Mean firing rates during locomotion and immobility**
562 To calculate the mean firing rates during locomotion, we counted the number of spikes during
563 locomotion periods and divided this number by the total duration of locomotion. Similarly, for mean
564 firing rates during immobility, we calculated the number of spikes that occurred during immobility
565 periods and divided this number by the total duration of immobility.
566
567 **Correlation between instantaneous firing rate and animal speed**
568 To estimate the instantaneous firing rates of individual neurons over time, we convolved their spike
569 trains with a Gaussian window of 250 ms. Subsequently, we calculated the Pearson correlation
570 coefficient between these instantaneous firing rates and the animal's speed for each neuron.
571
572 **Grand average cross-correlogram (CCG)**
573 Grand average CCGs were generated by constructing histograms of relative spike timings between

spikes of a reference cell and spikes of all other neurons in the same session as the target cell population. Histograms were binned using 1-ms time bins. Spike counts were normalized by the number of reference spikes times the number of all other neurons. An equal number of cells from different sessions were randomly selected to form the shuffled target cell population to assess the statistical significance of the CCG peaks. Subsequently, grand average CCGs were computed using shuffled spike trains for comparison. Grand average CCGs were calculated using all spikes in the 180-s recording periods, subsets of spikes during immobility periods (immobility grand average CCGs), and subsets of spikes during locomotion periods (locomotion grand average CCGs).

Detection of the population synchrony

To assess population synchrony, we counted the number of spikes from all neurons within a sliding window of 25 ms. To test the significance of the synchrony, we generated surrogate data by jittering spike timings within a ±75-ms window. By comparing the spike counts between the original and jittered populations, we determined population synchrony when the spike count was higher than the mean plus four standard deviations of the jittered spike counts. To estimate synchronous event rates, we divided the entire 180-s recordings into halves and calculated the event rate in each of the 90-s segments. Additionally, we quantified the ensemble sizes by counting the percentage of participating neurons in each synchronous event.

Pairwise cross-correlogram (CCG) of neuronal pairs

To compute the CCG, we first determined the time difference between spikes in the target and reference neurons and then binned these values into 1-ms time bins. CCGs were only computed for pairs with more than 100 counts within the CCG window of ±500 ms to ensure reliable correlation. We defined the peak of the CCG as the local maxima within ±30 ms of lag. To assess the significance of cross-correlations, we generated surrogate data by jittering the spike times of the target neuron

599 within a ±75 ms window. We computed the CCG peak for a thousand iterations and calculated p-
600 values by comparing the percentile of the peak in the null distribution of the jittered peak values.
601 The synchronization strength was estimated as the ratio between the original CCG peak and the
602 mean spike count of the same bin as the original CCG peak averaged across the jittered histograms.
603 For display purposes, the CCGs were smoothed using a 5-point moving average. CCGs were
604 calculated using all spikes in the 180-s recording periods, subsets of spikes during immobility
605 periods (immobility pairwise CCGs), and subsets of spikes during locomotion periods (locomotion
606 pairwise CCGs).
607
608 **LFP ripple analysis**
609 To detect ripples, we performed band-pass filtering of the LFP signal between 120 and 240 Hz,
610 followed by computing the envelope using the absolute values of the Hilbert transform, which was
611 then low-pass filtered at 20 Hz. The start and end times of ripples were identified by setting the
612 upper and lower thresholds at the mean plus 7 and 3.5 times the standard deviation of the
613 envelope, respectively. For a ripple event to be included, three conditions had to be met: (1) values
614 within the event were higher than the lower threshold, (2) at least one value exceeded the upper
615 threshold, and (3) the minimum duration of the event was 30 ms. The start and end times of a
616 ripple event were defined as the positive and negative crossings of the lower threshold,
617 respectively. We defined in-ripple periods as the time between the start and end of detected LFP
618 ripple events, while out-ripple periods were periods outside the in-ripple periods. The envelope
619 peak values of the detected ripple events were used as the time of ripple occurrence. These timings
620 were utilized as trigger timings to calculate averages triggered by ripples. Two co-occurrences were
621 quantified: the percentages of LFP ripple oscillations that occurred with synchronous ensembles
622 and the percentages of synchronous ensembles that occurred with LFP ripple oscillations.
623
624 **Ripple modulation index**

We utilized the ripple modulation index to assess changes in firing rates during ripples compared to periods outside ripples. This index was computed as the ratio of the difference in mean firing rates during in- and out-ripple periods to the sum of the mean firing rates during both periods. Specifically, we first calculated the mean firing rate during in-ripple periods and the mean firing rate during out-ripple periods. Next, we subtracted the mean firing rate during out-ripple periods from the mean firing rate during in-ripple periods and divided the result by the sum of the mean firing rates during both periods. The resulting ripple modulation index indicates the magnitude and direction of the firing rate modulation during ripple compared to periods outside ripples.

LFP traces triggered by population synchrony and analysis

The midpoints of the synchronous event intervals were utilized as triggers to align LFP traces. These traces were aligned within a ± 1-second window around the trigger time points. To calculate the spectral density functions of the aligned LFP traces, we performed a 16,384-point fast Fourier transform of the 2-second LFP traces. The power spectra were then estimated as the squared absolute values of the Fourier coefficients. Ripple power was calculated as the sum of the power distributed between 120 and 240 Hz. To calculate theta modulation strength and preferred angles of the synchronous ensembles, LFP was first filtered within the theta frequency range. Then, the phase $\varphi(t)$ and the instantaneous amplitude $A(t)$ of the filtered LFP were computed using the Hilbert transform. A vector $V_k = A(t_k)e^{i\varphi(t_k)}$ was assigned to each synchronous ensemble that occurred at time t_k. The modulation strength and the preferred phase angle were determined as the absolute value and the phase angle of the summed vector over all ensembles, respectively. Modulation strengths were normalized by the total length of all vectors.

Subthreshold membrane voltage (subVm)

To compute the subVm of individual neurons, we began by determining the difference between the raw dF/F signal and the high-pass version of dF/F. Next, we calculated the spike threshold for each

651 cell by identifying the voltage value corresponding to the peak of the first derivative of the spike
652 waveforms. Any fluorescence values in the slow dF/F time courses that surpassed the spike
653 thresholds were linearly interpolated.
654
655 **SubVm traces triggered by population synchrony**
656 The midpoint of the time intervals, during which synchronous ensembles were detected, served as
657 the reference points for aligning fluorescence traces within a $\pm$300 ms window around those
658 reference points. To eliminate any interference from membrane potential fluctuations associated
659 with spikes, we excluded aligned traces in cases where any spike occurred within the time intervals
660 of the aligned traces.
661
662 **SubVm theta modulation and phase preference of spikes occurred inside and outside the**
663 **population synchrony events**
664 The subVm was initially filtered within the theta frequency range. Subsequently, the phase $\varphi(t)$
665 and the instantaneous amplitude $A(t)$ of the filtered subVm were computed using the Hilbert
666 transform. Spikes were categorized into four groups: those occurring during or outside immobility
667 synchronous events and those occurring during or outside locomotion synchronous events. Within
668 each category, a vector $V_k = A(t_k)e^{i\varphi(t_k)}$ was assigned to each spike that occurred at time t_k.
669 The modulation strength and the preferred phase angle were determined as the absolute value and
670 the phase angle of the summed vector over all spikes, respectively. Modulation strengths were
671 normalized by the total length of all vectors to facilitate comparison between neurons.
672
673 **Spike-triggered fluorescence traces**
674 We extracted segments of fluorescence traces using a $\pm$300 ms time window centered on the spike
675 timings. To examine variations in fluorescence waveforms triggered by spikes within and outside
676 synchronous events, we categorized the fluorescence traces based on whether the spikes occurred

677 within or outside these events. Subsequently, we performed pairwise comparisons of the
678 fluorescence values from the same neuron, concentrating on spikes occurring during corresponding
679 behavioral states. Neurons with fewer than four triggering events in any of these categories were
680 omitted from the analysis.
681
682 **Cross-correlation and coherence analysis to the subVm traces**
683 To calculate cross-correlation and theta coherence of subVm between pairs of neurons during
684 locomotion and immobility, we initially divided the 180-second subVm traces into 1-second
685 segments with a 50% overlap. These segments were then categorized into the locomotion group if
686 the animal's speed remained above three cm/s for more than 90% of the time within that segment.
687 Similarly, segments were sorted into the immobility group if the animal's speed remained below
688 one cm/s for more than 90% of the time within that segment. Subsequently, we computed the
689 cross-correlation and magnitude-squared coherence function of frequency for pairs of co-occurred
690 segments belonging to a specific cell pair. Mean cross-correlations of individual cell pairs were
691 averaged across segments that occurred in the same behavioral states (i.e., locomotion or
692 immobility states). To estimate theta coherence, we averaged the values of the coherence function
693 within the theta frequency range (4-12 Hz). Theta coherences from the same cell pair during the
694 same behavioral state were pooled together, and the average was used as an estimate for the theta
695 coherence of that cell pair during a particular behavioral state. Finally, Spearman correlation
696 coefficients were calculated between the mean theta coherences of cell pairs and their soma
697 distances.
698
699 **Spatial analysis**
700 We partitioned a 90-cm-long track into 36 spatial bins to analyze spatial tuning properties. For each
701 cell, the spatial tuning curve was computed by determining the mean firing rate, defined as the
702 number of spikes within the bin when the animal's speed exceeded three cm/s, divided by the total

703 dwell times using the same speed threshold. The peak firing rates were identified as the maximal
704 rate on the spatial tuning curve. Spatial selectivity was calculated as one minus the circular variance
705 of the spatial tuning curve. Neurons were classified as place cells when their spatial selectivity
706 exceeded 0.25, and peak firing rates exceeded 1 Hz. To assess the similarity of spatial tuning
707 between pairs of neurons, Spearman correlation coefficients were calculated for the spatial tuning
708 curves. To explore the relationship between levels of synchronization and spatial tuning similarity
709 among pairs of place cells, Spearman correlation coefficients were computed between
710 synchronization strengths of cell pairs and correlation coefficients of their spatial tuning curves.
711
712 **Data analysis and statistics**
713 Data analysis was performed using MATLAB (Mathworks, R2019b), and results were presented as
714 standard error of the mean unless otherwise specified. Boxplots were used to depict the median,
715 first quartile, and third quartile, with the middle line, the upper edge, and the lower edge of the
716 box, respectively. The whiskers of the boxplots represented the 5th and 95th percentiles of the
717 distribution.
718

1 Takeuchi, T., Duszkiewicz, A. J. & Morris, R. G. The synaptic plasticity and memory hypothesis: encoding, storage and persistence. *Philos Trans R Soc Lond B Biol Sci* **369**, 20130288 (2014). https://doi.org:10.1098/rstb.2013.0288

2 Moser, M. B., Rowland, D. C. & Moser, E. I. Place cells, grid cells, and memory. *Cold Spring Harb Perspect Biol* **7**, a021808 (2015). https://doi.org:10.1101/cshperspect.a021808

3 Axmacher, N., Mormann, F., Fernandez, G., Elger, C. E. & Fell, J. Memory formation by neuronal synchronization. *Brain Res Rev* **52**, 170-182 (2006). https://doi.org:10.1016/j.brainresrev.2006.01.007

4 Paulsen, O. & Sejnowski, T. J. Natural patterns of activity and long-term synaptic plasticity. *Curr Opin Neurobiol* **10**, 172-179 (2000). https://doi.org:10.1016/s0959-4388(00)00076-3

5 Wang, X. J. Neurophysiological and computational principles of cortical rhythms in cognition. *Physiol Rev* **90**, 1195-1268 (2010). https://doi.org:10.1152/physrev.00035.2008

6 Harris, K. D., Csicsvari, J., Hirase, H., Dragoi, G. & Buzsaki, G. Organization of cell assemblies in the hippocampus. *Nature* **424**, 552-556 (2003). https://doi.org:10.1038/nature01834

7 Squire, L. R. & Wixted, J. T. The cognitive neuroscience of human memory since H.M. *Annu Rev Neurosci* **34**, 259-288 (2011). https://doi.org:10.1146/annurev-neuro-061010-113720

8 Buzsaki, G. Hippocampal sharp wave-ripple: A cognitive biomarker for episodic memory and planning. *Hippocampus* **25**, 1073-1188 (2015). https://doi.org:10.1002/hipo.22488

9 Nadasdy, Z., Hirase, H., Czurko, A., Csicsvari, J. & Buzsaki, G. Replay and time compression of recurring spike sequences in the hippocampus. *J Neurosci* **19**, 9497-9507 (1999). https://doi.org:10.1523/JNEUROSCI.19-21-09497.1999

10 Cheng, S. & Frank, L. M. New experiences enhance coordinated neural activity in the hippocampus. *Neuron* **57**, 303-313 (2008). https://doi.org:10.1016/j.neuron.2007.11.035

11 Dragoi, G. & Tonegawa, S. Preplay of future place cell sequences by hippocampal cellular assemblies. *Nature* **469**, 397-401 (2011). https://doi.org:10.1038/nature09633

12 Liu, C., Todorova, R., Tang, W., Oliva, A. & Fernandez-Ruiz, A. Associative and predictive hippocampal codes support memory-guided behaviors. *Science* **382**, eadi8237 (2023). https://doi.org:10.1126/science.adi8237

13 Colgin, L. L. Rhythms of the hippocampal network. *Nat Rev Neurosci* **17**, 239-249 (2016). https://doi.org:10.1038/nrn.2016.21

14 Buzsaki, G. & Silva, F. L. High frequency oscillations in the intact brain. *Prog Neurobiol* **98**, 241-249 (2012). https://doi.org:10.1016/j.pneurobio.2012.02.004

15 Csicsvari, J., Hirase, H., Czurko, A. & Buzsaki, G. Reliability and state dependence of pyramidal cell-interneuron synapses in the hippocampus: an ensemble approach in the behaving rat. *Neuron* **21**, 179-189 (1998). https://doi.org:10.1016/s0896-6273(00)80525-5

16 Gillespie, A. K. *et al.* Hippocampal replay reflects specific past experiences rather than a plan for subsequent choice. *Neuron* **109**, 3149-3163 e3146 (2021). https://doi.org:10.1016/j.neuron.2021.07.029

17 Yagi, S., Igata, H., Ikegaya, Y. & Sasaki, T. Awake hippocampal synchronous events are incorporated into offline neuronal reactivation. *Cell Rep* **42**, 112871 (2023). https://doi.org:10.1016/j.celrep.2023.112871

18 El-Gaby, M. *et al.* An emergent neural coactivity code for dynamic memory. *Nat Neurosci* **24**, 694-704 (2021). https://doi.org:10.1038/s41593-021-00820-w

19 Skaggs, W. E., McNaughton, B. L., Wilson, M. A. & Barnes, C. A. Theta phase precession in hippocampal neuronal populations and the compression of temporal sequences. *Hippocampus* **6**, 149-172 (1996). https://doi.org:10.1002/(SICI)1098-1063(1996)6:2<149::AID-HIPO6>3.0.CO;2-K

20 Dragoi, G. & Buzsaki, G. Temporal encoding of place sequences by hippocampal cell assemblies. *Neuron* **50**, 145-157 (2006). https://doi.org:10.1016/j.neuron.2006.02.023

21 Foster, D. J. & Wilson, M. A. Hippocampal theta sequences. *Hippocampus* **17**, 1093-1099 (2007). https://doi.org:10.1002/hipo.20345

22 Mizuseki, K. & Buzsaki, G. Theta oscillations decrease spike synchrony in the hippocampus and entorhinal cortex. *Philos Trans R Soc Lond B Biol Sci* **369**, 20120530 (2014). https://doi.org:10.1098/rstb.2012.0530

23 O'Keefe, J. & Recce, M. L. Phase relationship between hippocampal place units and the EEG theta rhythm. *Hippocampus* **3**, 317-330 (1993). https://doi.org:10.1002/hipo.450030307

24 Lee, A. K. & Brecht, M. Elucidating Neuronal Mechanisms Using Intracellular Recordings during Behavior. *Trends Neurosci* **41**, 385-403 (2018). https://doi.org:10.1016/j.tins.2018.03.014

25 Petersen, C. C. H. Whole-Cell Recording of Neuronal Membrane Potential during Behavior. *Neuron* **95**, 1266-1281 (2017). https://doi.org:10.1016/j.neuron.2017.06.049

26 Giocomo, L. M., Zilli, E. A., Fransen, E. & Hasselmo, M. E. Temporal frequency of subthreshold oscillations scales with entorhinal grid cell field spacing. *Science* **315**, 1719-1722 (2007). https://doi.org:10.1126/science.1139207

27 Lampl, I., Reichova, I. & Ferster, D. Synchronous membrane potential fluctuations in neurons of the cat visual cortex. *Neuron* **22**, 361-374 (1999). https://doi.org:10.1016/s0896-6273(00)81096-x

28 Poulet, J. F. & Petersen, C. C. Internal brain state regulates membrane potential synchrony in barrel cortex of behaving mice. *Nature* **454**, 881-885 (2008). https://doi.org:10.1038/nature07150

29 Abdelfattah, A. S. *et al.* Sensitivity optimization of a rhodopsin-based fluorescent voltage indicator. *Neuron* (2023). https://doi.org:10.1016/j.neuron.2023.03.009

30 Adam, Y. *et al.* Voltage imaging and optogenetics reveal behaviour-dependent changes in hippocampal dynamics. *Nature* **569**, 413-417 (2019). https://doi.org:10.1038/s41586-019-1166-7

31 Klausberger, T. *et al.* Brain-state- and cell-type-specific firing of hippocampal interneurons in vivo. *Nature* **421**, 844-848 (2003). https://doi.org:10.1038/nature01374

32 Rolotti, S. V. *et al.* Local feedback inhibition tightly controls rapid formation of hippocampal place fields. *Neuron* **110**, 783-794 e786 (2022). https://doi.org:10.1016/j.neuron.2021.12.003

33 Sheffield, M. E. J., Adoff, M. D. & Dombeck, D. A. Increased Prevalence of Calcium Transients across the Dendritic Arbor during Place Field Formation. *Neuron* **96**, 490-504 e495 (2017). https://doi.org:10.1016/j.neuron.2017.09.029

34 Takacs, V. T., Klausberger, T., Somogyi, P., Freund, T. F. & Gulyas, A. I. Extrinsic and local glutamatergic inputs of the rat hippocampal CA1 area differentially innervate pyramidal cells and interneurons. *Hippocampus* **22**, 1379-1391 (2012). https://doi.org:10.1002/hipo.20974

35 English, D. F. *et al.* Pyramidal Cell-Interneuron Circuit Architecture and Dynamics in Hippocampal Networks. *Neuron* **96**, 505-520 e507 (2017). https://doi.org:10.1016/j.neuron.2017.09.033

36 Maccaferri, G., Roberts, J. D., Szucs, P., Cottingham, C. A. & Somogyi, P. Cell surface domain specific postsynaptic currents evoked by identified GABAergic neurones in rat hippocampus in vitro. *J Physiol* **524 Pt 1**, 91-116 (2000). https://doi.org:10.1111/j.1469-7793.2000.t01-3-00091.x

37 Geiller, T. *et al.* Local circuit amplification of spatial selectivity in the hippocampus. *Nature* **601**, 105-109 (2022). https://doi.org:10.1038/s41586-021-04169-9

38 Trouche, S. *et al.* Recoding a cocaine-place memory engram to a neutral engram in the hippocampus. *Nat Neurosci* **19**, 564-567 (2016). https://doi.org:10.1038/nn.4250

39 Go, M. A. *et al.* Place Cells in Head-Fixed Mice Navigating a Floating Real-World Environment. *Front Cell Neurosci* **15**, 618658 (2021). https://doi.org:10.3389/fncel.2021.618658

40 Kramis, R., Vanderwolf, C. H. & Bland, B. H. Two types of hippocampal rhythmical slow activity in both the rabbit and the rat: relations to behavior and effects of atropine, diethyl ether, urethane, and pentobarbital. *Exp Neurol* **49**, 58-85 (1975). https://doi.org:10.1016/0014-4886(75)90195-8

41 Bland, B. H. The physiology and pharmacology of hippocampal formation theta rhythms. *Prog Neurobiol* **26**, 1-54 (1986). https://doi.org:10.1016/0301-0082(86)90019-5

42 Buzsaki, G. Theta oscillations in the hippocampus. *Neuron* **33**, 325-340 (2002). https://doi.org:10.1016/s0896-6273(02)00586-x

43 Sainsbury, R. S., Heynen, A. & Montoya, C. P. Behavioral correlates of hippocampal type 2 theta in the rat. *Physiol Behav* **39**, 513-519 (1987). https://doi.org:10.1016/0031-9384(87)90382-9

44 Sainsbury, R. S. Hippocampal theta: a sensory-inhibition theory of function. *Neurosci Biobehav Rev* **22**, 237-241 (1998). https://doi.org:10.1016/s0149-7634(97)00011-0

45 Barry, C., Heys, J. G. & Hasselmo, M. E. Possible role of acetylcholine in regulating spatial novelty effects on theta rhythm and grid cells. *Front Neural Circuits* **6**, 5 (2012). https://doi.org:10.3389/fncir.2012.00005

46 Nakajima, Y., Nakajima, S., Leonard, R. J. & Yamaguchi, K. Acetylcholine raises excitability by inhibiting the fast transient potassium current in cultured hippocampal neurons. *Proc Natl*

Acad Sci U S A **83**, 3022-3026 (1986). https://doi.org:10.1073/pnas.83.9.3022

47 Markram, H. & Segal, M. Acetylcholine potentiates responses to N-methyl-D-aspartate in the rat hippocampus. *Neurosci Lett* **113**, 62-65 (1990). https://doi.org:10.1016/0304-3940(90)90495-u

48 Fraser, D. D. & MacVicar, B. A. Cholinergic-dependent plateau potential in hippocampal CA1 pyramidal neurons. *J Neurosci* **16**, 4113-4128 (1996). https://doi.org:10.1523/JNEUROSCI.16-13-04113.1996

49 Toth, K., Freund, T. F. & Miles, R. Disinhibition of rat hippocampal pyramidal cells by GABAergic afferents from the septum. *J Physiol* **500 (Pt 2)**, 463-474 (1997). https://doi.org:10.1113/jphysiol.1997.sp022033

50 Colgin, L. L. Mechanisms and functions of theta rhythms. *Annu Rev Neurosci* **36**, 295-312 (2013). https://doi.org:10.1146/annurev-neuro-062012-170330

51 Cobb, S. R., Buhl, E. H., Halasy, K., Paulsen, O. & Somogyi, P. Synchronization of neuronal activity in hippocampus by individual GABAergic interneurons. *Nature* **378**, 75-78 (1995). https://doi.org:10.1038/378075a0

52 Stark, E. *et al.* Inhibition-induced theta resonance in cortical circuits. *Neuron* **80**, 1263-1276 (2013). https://doi.org:10.1016/j.neuron.2013.09.033

53 Landfield, P. W., McGaugh, J. L. & Tusa, R. J. Theta rhythm: a temporal correlate of memory storage processes in the rat. *Science* **175**, 87-89 (1972). https://doi.org:10.1126/science.175.4017.87

54 Berry, S. D. & Thompson, R. F. Prediction of learning rate from the hippocampal electroencephalogram. *Science* **200**, 1298-1300 (1978). https://doi.org:10.1126/science.663612

55 Belchior, H., Lopes-Dos-Santos, V., Tort, A. B. & Ribeiro, S. Increase in hippocampal theta oscillations during spatial decision making. *Hippocampus* **24**, 693-702 (2014). https://doi.org:10.1002/hipo.22260

56 Winson, J. Loss of hippocampal theta rhythm results in spatial memory deficit in the rat. *Science* **201**, 160-163 (1978). https://doi.org:10.1126/science.663646

57 Mitchell, S. J., Rawlins, J. N., Steward, O. & Olton, D. S. Medial septal area lesions disrupt theta rhythm and cholinergic staining in medial entorhinal cortex and produce impaired radial arm maze behavior in rats. *J Neurosci* **2**, 292-302 (1982). https://doi.org:10.1523/JNEUROSCI.02-03-00292.1982

58 Mizumori, S. J., Perez, G. M., Alvarado, M. C., Barnes, C. A. & McNaughton, B. L. Reversible inactivation of the medial septum differentially affects two forms of learning in rats. *Brain research* **528**, 12-20 (1990). https://doi.org:10.1016/0006-8993(90)90188-h

59 M'Harzi, M. & Jarrard, L. E. Effects of medial and lateral septal lesions on acquisition of a place and cue radial maze task. *Behav Brain Res* **49**, 159-165 (1992). https://doi.org:10.1016/s0166-4328(05)80160-3

871 60 Wang, Y., Romani, S., Lustig, B., Leonardo, A. & Pastalkova, E. Theta sequences are essential
872 for internally generated hippocampal firing fields. *Nat Neurosci* **18**, 282-288 (2015).
873 https://doi.org:10.1038/nn.3904
874 61 McNaughton, N., Ruan, M. & Woodnorth, M. A. Restoring theta-like rhythmicity in rats
875 restores initial learning in the Morris water maze. *Hippocampus* **16**, 1102-1110 (2006).
876 https://doi.org:10.1002/hipo.20235
877 62 Lee, D. J. *et al.* Medial septal nucleus theta frequency deep brain stimulation improves spatial
878 working memory after traumatic brain injury. *J Neurotrauma* **30**, 131-139 (2013).
879 https://doi.org:10.1089/neu.2012.2646
880 63 Hasselmo, M. E., Bodelon, C. & Wyble, B. P. A proposed function for hippocampal theta rhythm:
881 separate phases of encoding and retrieval enhance reversal of prior learning. *Neural Comput*
882 **14**, 793-817 (2002). https://doi.org:10.1162/089976602317318965
883 64 Rutishauser, U., Ross, I. B., Mamelak, A. N. & Schuman, E. M. Human memory strength is
884 predicted by theta-frequency phase-locking of single neurons. *Nature* **464**, 903-907 (2010).
885 https://doi.org:10.1038/nature08860
886 65 Siegle, J. H. & Wilson, M. A. Enhancement of encoding and retrieval functions through theta
887 phase-specific manipulation of hippocampus. *Elife* **3**, e03061 (2014).
888 https://doi.org:10.7554/eLife.03061
889 66 Vandecasteele, M. *et al.* Optogenetic activation of septal cholinergic neurons suppresses
890 sharp wave ripples and enhances theta oscillations in the hippocampus. *Proc Natl Acad Sci U*
891 *S A* **111**, 13535-13540 (2014). https://doi.org:10.1073/pnas.1411233111
892 67 Valero, M. *et al.* Determinants of different deep and superficial CA1 pyramidal cell dynamics
893 during sharp-wave ripples. *Nat Neurosci* **18**, 1281-1290 (2015).
894 https://doi.org:10.1038/nn.4074
895 68 Deuchars, J. & Thomson, A. M. CA1 pyramid-pyramid connections in rat hippocampus in vitro:
896 dual intracellular recordings with biocytin filling. *Neuroscience* **74**, 1009-1018 (1996).
897 https://doi.org:10.1016/0306-4522(96)00251-5
898 69 Caporale, N. & Dan, Y. Spike timing-dependent plasticity: a Hebbian learning rule. *Annu Rev*
899 *Neurosci* **31**, 25-46 (2008). https://doi.org:10.1146/annurev.neuro.31.060407.125639
900 70 Markram, H., Lubke, J., Frotscher, M. & Sakmann, B. Regulation of synaptic efficacy by
901 coincidence of postsynaptic APs and EPSPs. *Science* **275**, 213-215 (1997).
902 https://doi.org:10.1126/science.275.5297.213
903 71 Bi, G. Q. & Poo, M. M. Synaptic modifications in cultured hippocampal neurons: dependence
904 on spike timing, synaptic strength, and postsynaptic cell type. *J Neurosci* **18**, 10464-10472
905 (1998). https://doi.org:10.1523/JNEUROSCI.18-24-10464.1998
906 72 Ali, A. B., Deuchars, J., Pawelzik, H. & Thomson, A. M. CA1 pyramidal to basket and bistratified
907 cell EPSPs: dual intracellular recordings in rat hippocampal slices. *J Physiol* **507 (Pt 1)**, 201-217
908 (1998). https://doi.org:10.1111/j.1469-7793.1998.201bu.x

73 Ali, A. B. & Thomson, A. M. Facilitating pyramid to horizontal oriens-alveus interneurone inputs: dual intracellular recordings in slices of rat hippocampus. *J Physiol* **507 (Pt 1)**, 185-199 (1998). https://doi.org:10.1111/j.1469-7793.1998.185bu.x

74 Engel, A. K., Konig, P., Kreiter, A. K. & Singer, W. Interhemispheric synchronization of oscillatory neuronal responses in cat visual cortex. *Science* **252**, 1177-1179 (1991). https://doi.org:10.1126/science.252.5009.1177

75 Alonso, J. M., Usrey, W. M. & Reid, R. C. Precisely correlated firing in cells of the lateral geniculate nucleus. *Nature* **383**, 815-819 (1996). https://doi.org:10.1038/383815a0

76 Zheng, Q. *et al.* Rational Design of Fluorogenic and Spontaneously Blinking Labels for Super-Resolution Imaging. *ACS Cent Sci* **5**, 1602-1613 (2019). https://doi.org:10.1021/acscentsci.9b00676

Acknowledgments

We express our sincere gratitude to Dr. Luke Lavis for sharing the JF_{552}-HaloTag ligand. Special thanks to Mr. Yu-Ting Lin and Ms. Hui-Ching Chen for technical assistance. We are grateful to Drs. Shih-Chieh Lin, Kuo-Hua Huang, Shi-Bing Yang, and Fu-Chin Liu for their insightful comments on the manuscript.

Funding statements

National Science and Technology Council, Taiwan (B.-J.L. and T.-W.C.)
Howard Hughes Medical Institute, USA (E.R.S.)

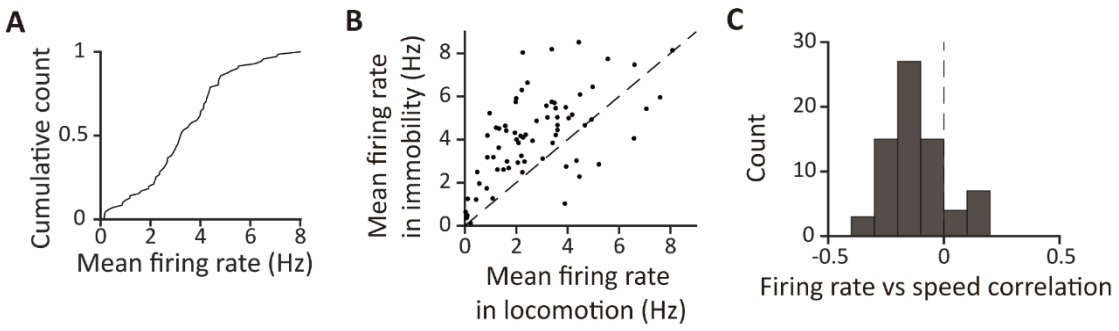

Supplementary Figure 1 Mean firing rate distribution and correlation with animals' speed.

(A) Cumulative distribution of mean firing rates averaged throughout the entire 180-second recording period.

(B) Mean firing rates during locomotion plotted against mean firing rates during immobility for individual cells. Each dot represents a cell. Mean firing rates are higher during immobility than during locomotion (4.2±0.2 Hz for immobility, 2.8±0.2 Hz for locomotion, n=71 cells, $p<0.001$, Wilcoxon signed-rank test).

(C) Histogram of correlation coefficients between instantaneous firing rates and the animals' speed for each neuron.

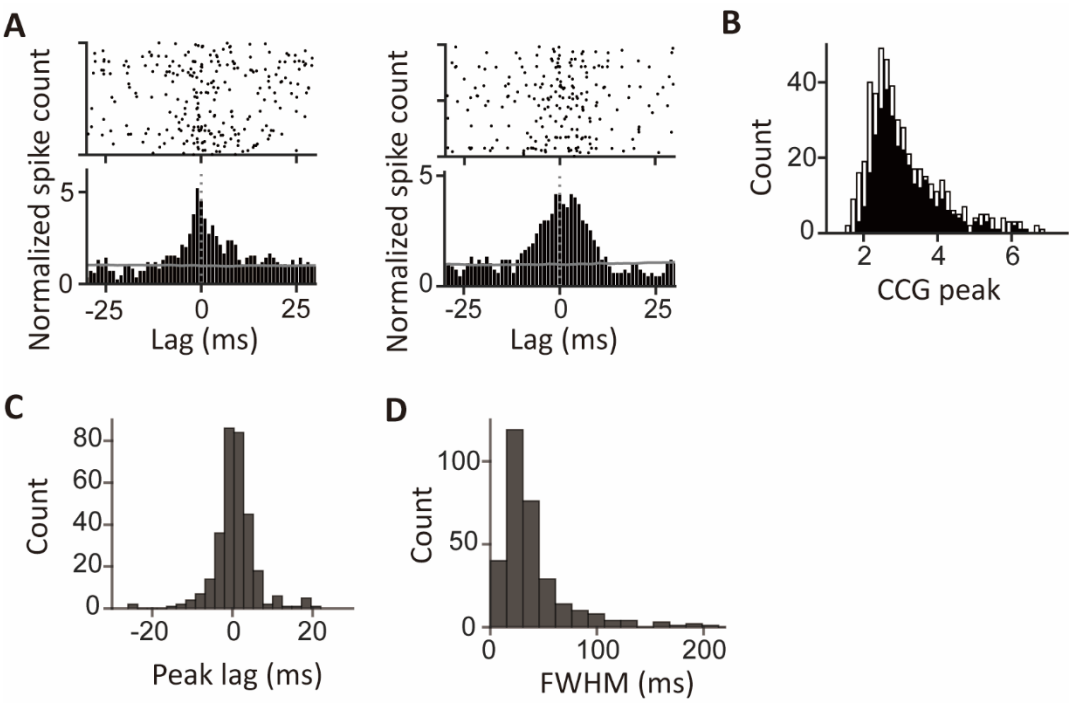

Figure 1-figure supplement 1 Pairwise cross-correlogram (CCG) between CA1 pyramidal cells.

(A) CCGs of two representative cell pairs exhibiting significant peaks compared to the jittered spike trains of the target cells (gray lines).

(B) Distribution of the CCG peaks (n=497 pairs). Black: CCG peaks with significance ($p<0.05$). White: CCG peaks without significance ($p>=0.05$).

(C) Histogram of peak lags of significant CCG peaks (n=315 pairs).

(D) Histogram of FWHMs of significant CCG peaks (n=315 pairs).

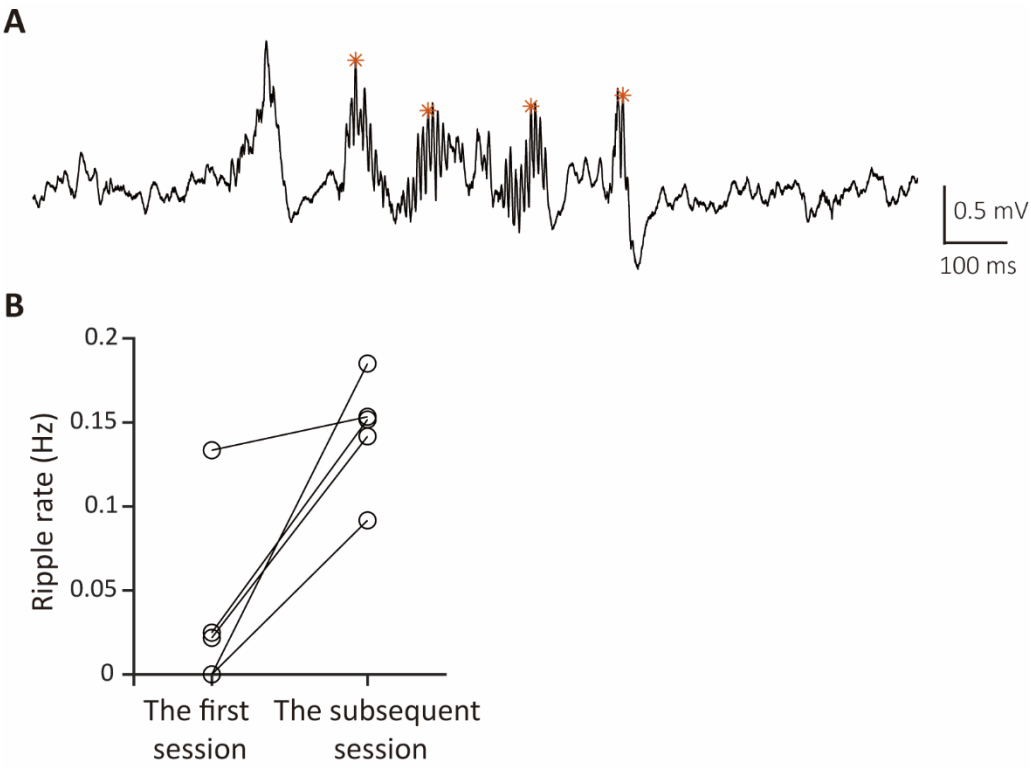

Figure 3-figure supplement 1 LFP ripples recorded in the first and subsequent sessions in a novel maze. (A) An example LFP trace with ripples recorded in a subsequent session following the first session of novel exploration, where no ripple was detected.

(B) Ripple rates in the first and subsequent sessions recorded in the same animals (n=5 mice) during novel exploration.

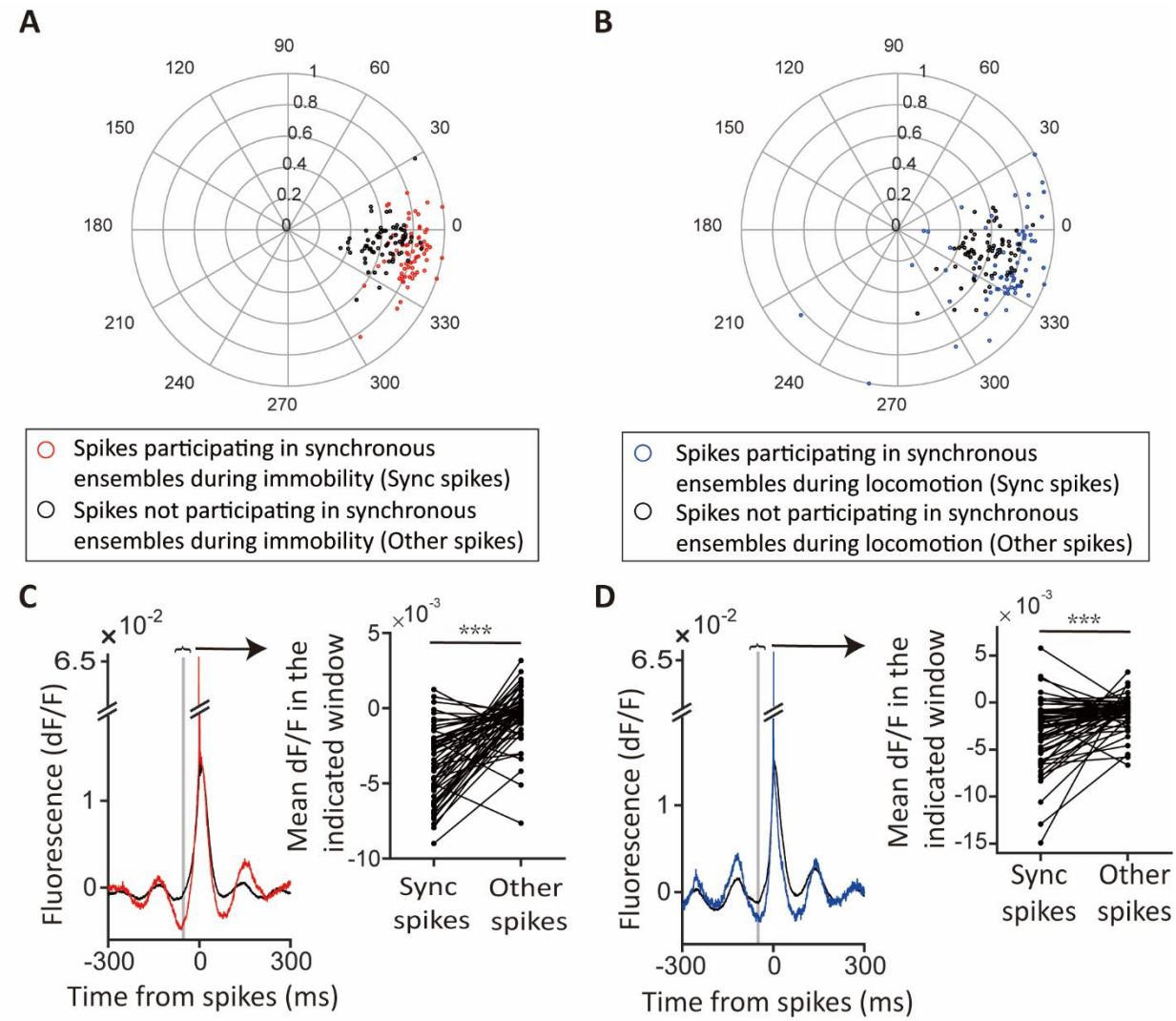

958

959 **Figure 4-figure supplement 1 Theta modulation of spikes during immobility and locomotion**

960 **periods of novel exploration.**

961 **(A)** Polar plot comparing theta modulation between spikes participating in synchronous ensembles

962 (sync spikes) and spikes not participating in synchronous ensembles (other spikes) during

963 immobility. Each dot represents the averaged modulation of a cell. The modulation strengths of

964 spikes participating in synchrony are significantly higher than those of spikes not participating in

965 synchrony (modulation strength for spikes participating in synchronous ensembles: 0.81±0.08, for

966 spikes not participating in synchronous ensembles: 0.63±0.12, mean±s.d., n=71 cells, $p<0.001$, pair

967 Student's *t*-test).

968 **(B)** Same as in (A), but during locomotion (modulation strength for spikes participating in

synchronous ensembles: 0.76±0.18, for spikes not participating in synchronous ensembles: 0.60± 0.12, mean±s.d., n=71 cells, $p<0.001$, pair Student's *t*-test).

(C) Average fluorescence triggered by cells' spikes participating in synchronous ensembles (red, sync spikes) and not participating in synchronous ensembles during immobility (black, other spikes; n=59 cells). Inset: Pairwise comparison of average fluorescence 50±5 ms before time of spikes (t=0) between the two triggered groups (n=59 cells).

(D) Same as in (C), but during locomotion.

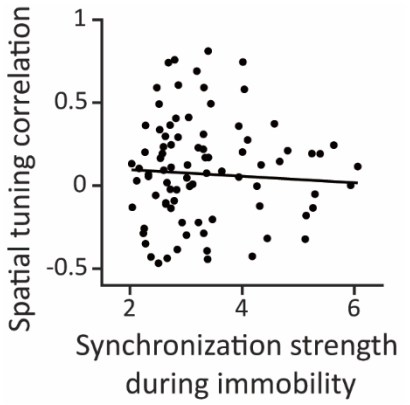

Figure 5-figure supplement 1 Synchronization strengths during immobility show little correlation with the similarity of spatial tunings between place cells. Synchronization strengths during immobility plotted against correlation coefficients of spatial tunings for pairs of place cells. Synchronization strengths show little correlation with similarities of spatial tunings (Spearman correlation coefficient=-0.003, p=0.98, n=88 cell pairs).